

Data-driven modeling of the aerodynamic deformation and drag for a freely moving drop in the sub-critical Weber number regime

T. Mahmood^a, A. Tonmoy^b, C. Severt^b, Y. Wang^b, Y. Ling^{b,*}

^a*Department of Mechanical Engineering, Baylor University, Waco, Texas, 76798, USA*

^b*Department of Mechanical Engineering, University of South Carolina, Columbia, South Carolina, 29208, USA*

Abstract

Accurate prediction of the dynamics and deformation of freely moving drops is crucial for numerous droplet applications. When the Weber number is finite but below a critical value, the drop deviates from its spherical shape and deforms as it is accelerated by the gas stream. Since aerodynamic drag on the drop depends on its shape oscillation, accurately modeling the drop shape evolution is essential for predicting the drop's velocity and position. In this study, 2D axisymmetric interface-resolved simulations were performed to provide a comprehensive dataset for developing a data-driven model. Parametric simulations were conducted by systematically varying the drop diameter and free-stream velocity, achieving wide ranges of Weber and Reynolds numbers. The instantaneous drop shapes obtained in simulations are characterized by spherical harmonics. Temporal data of the drag and modal coefficients are collected from the simulation data to train a Nonlinear Auto-Regressive models with eXogenous inputs (NARX) neural network model. The overall model consists of two multi-layer perceptron networks, which predict the modal coefficients and the drop drag, respectively. The drop shape can be reconstructed with the predicted modal coefficients. The model predictions are validated against the simulation data in the testing set, showing excellent agreement for the evolutions of both the drop

*Corresponding author.

Email address: Stanley_Ling@sc.edu (Y. Ling)

shape and drag.

Keywords: Aerodynamic deformation, Machine-learning model, Drop oscillation, Drag model

1. Introduction

Accurate prediction of the dynamics of freely moving drops is important in numerous droplet applications, such as raindrop impact on aerodynamic surfaces, fuel injection, and spray cooling. Though the interaction between a drop and the surrounding gas flow is complex, the aerodynamic deformation of a drop is typically formulated in an ideal configuration, i.e., an initially stationary and spherical drop is suddenly exposed to an unbounded uniform gas stream [48, 27, 16]. In such cases, the drop deformation and dynamics are fully determined by the densities and viscosities of the drop liquid and the gas, ρ_l , μ_l , ρ_g , and μ_g , the surface tension σ , the initial drop diameter D_0 , and the gas stream velocity U_0 . The subscripts g and l are used to denote the properties for the gas and liquid, respectively, while the subscript 0 is used to represent the initial state. Neglecting the compressibility [49, 50, 43] and non-Newtonian [17, 51] effects, the drop shape deformation and dynamics can be fully characterized by four independent dimensionless parameters: the Weber number $We = \rho_g U_0^2 D_0 / \sigma$, the Reynolds number $Re = \rho_g U_0 D_0 / \mu_g$, the Ohnesorge number $Oh = \mu_l / \sqrt{\rho_l D_0 \sigma}$, and the gas-to-liquid density ratio $r = \rho_g / \rho_l$ [33, 14, 17, 11]. Except for high-pressure applications [26], the density ratio between gas and liquids is generally small and the effect of r is secondary [27]. The Ohnesorge number Oh measures the relative importance of liquid viscosity compared to surface tension. For low-viscosity liquids like water, Oh is generally small except for very small drops, and therefore surface tension is the dominant force to resist drop deformation or breakup. Previous studies showed that the effect of Oh on the criteria for the onset of breakup is small when $Oh < 0.1$ [14]. The Weber number We is generally used to characterize drop breakup criteria and breakup modes [14]. For water drops in air, the critical Weber number is

about 11, under which a drop will only experience shape oscillation but will not break. The Reynolds number Re dictates the viscous gas flows in outside the drop, such as the boundary layer separation and the wake structure. For a spherical particle, the wake becomes turbulent when $Re > 3000$ [57, 52].

In the sub-critical Weber number regime, the drop experiences shape oscillation when it is accelerated by the aerodynamic drag. The complex interaction between the shape oscillation and the surrounding flow makes accurate prediction of the drop shape and drag challenging. The oscillation dynamics for drops with finite We is more complicated than capillary oscillation of a drop in a quiescent environment [37, 20, 38, 30, 35]. As the drop experiences a large-amplitude oscillation, the nonlinear effect will modulate the drop oscillation dynamics [53, 5], e.g., the drop oscillation frequency decreases as the oscillation amplitude increases. Furthermore, the drop oscillation amplitude decreases over time due to viscous dissipation, so the nonlinear effect will be reduced as time elapses and as a result, the drop oscillation frequency will change over time. As the external gas flow and the liquid flow inside the drop can be significantly modulated by the drop shape oscillations [8, 19, 58], the drag coefficient for a deforming drop will be significantly different from a spherical drop in the zero- We limit, and will evolve in time in an oscillatory manner. How to incorporate the effect of shape oscillation in the drop drag model remains an open question [23].

In practical simulations of sprays consisting of a large number of droplets, it is impractical to resolve the interface of each individual drop. Instead, the drops are represented by point particles and traced in a Lagrangian framework [2, 32, 4]. The drop drag and shape deformation, along with other physics like heat and mass transfer between the drop and the surrounding flow [1, 10, 9] and aerodynamic breakup, need to be represented by subgrid models [31, 14]. For drops with finite We , traditional drag models for spherical drops [28] in the zero- We limit will be invalid. Though different physics-based models have been proposed [31, 18, 39, 15], significant discrepancies between the model predictions and high-fidelity simulation and experiment were observed [24]. The

fundamental challenge of physics-based models lies in the necessary assumptions/simplifications of the drop shape and surrounding flows, such as assuming the drop shape is a spheroid, which are typically valid only for a limited time period and small We .

Data-driven modeling is an important alternative to develop sub-scale models for multi-phase flows, and its capability is significantly enhanced by the rapid development of machine-learning techniques. Wan et al. [56] presented a data-driven kinematic model to predict the trajectories of bubbles in high- Re fluid flow using a recurrent neural network consisting of long short-term memory (LSTM) layers. Studies have been dedicated to developing machine-learning models of quasi-steady drag for particle-laden flow with finite particle volume fractions [13, 45, 46, 44]. To the knowledge of the authors, there are not yet machine-learning models for the drag force acting on deforming drops. The additional time-dependent shape deformation of drops makes the modeling more challenging compared to the particle counterpart.

The goal of the present study is to develop a data-driven model to predict the time evolutions of drop shape and drag for a freely-moving drop in the sub-critical Weber number regime. Though it is of highly interest to model a wider range of parameters that cover also the aerodynamic breakup of drops, the present study will be focused on the aerodynamic deformation of drops that will not experience breakup. To provide the data to train and to test the model, interface-resolved simulations using volume-of-fluid (VOF) method will be performed. The Nonlinear Auto-Regressive models with eXogenous inputs (NARX) recurrent neural network [21, 22] will be used to develop the data-driven models. The rest of the paper will be organized as follows. We will first define the problem and the parameter space of interest in section 2. The numerical methods and solver for the interface-resolved simulations will be presented in section 3, followed by the simulation results shown in section 4. The machine-learning model architecture will be described in section 5, and the model predictions and comparison with simulation data will be presented in section 6. Finally, we will conclude key findings of the present study in section 7.

2. Problem description and parameter space

2.1. Parameter space of interest

In the present study, we consider that an initially stationary and spherical drop is suddenly exposed to a uniform gas stream [36, 14, 47, 24]. The physical parameters and the dimensionless parameters are listed in Tables 1 and 2. The drop liquid and gas are taken to be water and air, respectively. As a result, $r = 0.0012$ is fixed and for such a low value the density ratio effect is negligible [27]. A parametric study is performed by varying U_0 and D_0 . As a result, We , Oh and Re vary from case to case. For the ranges of U_0 and D_0 considered, $Oh \leq 0.086$, and it is expected that the effect of liquid viscosity, though is present, is less important compared to surface tension. Previous studies indicated that the impact of Oh on the critical Weber number We_{cr} is negligible for the present ranges of r and Oh , and $We_{cr} \approx 11 \pm 2$ [14]. Furthermore, the drop drag mainly depends on Re , therefore, We and Re are the key controlling parameters. The ranges of which considered in the present study are : $0.1 \leq We \leq 10$ and $10 \leq Re \leq 1000$. The focus is on the sub-critical regime, $We < We_{cr}$, so that the drop will only undergo oscillation but will not break and form child droplets. Furthermore, we have only considered moderate Re so that the less expensive 2D axisymmetric simulations will remain good approximation, and neglecting the 3D flow features in the drop wake will not lead to significant effect on the drop deformation and drag [9]. The low computational costs for 2D axisymmetric simulations will allow us to consider a large number cases. To guarantee the compressibility effect is negligible, it is taken that $M < 0.3$, which leads to a constraint that $Re > 38.87 We$. Furthermore, we consider the drop diameter to be smaller than 10 mm, which then leads to another boundary in the $Re-We$ space, *i.e.*, $Re < 1632\sqrt{We}$. The final parameter space of interest is shown in Fig. 1(b).

2.2. Cases of study

A total of 102 cases were selected by performing a Latin Hypercube Sampling using the maximum-minimum distance criteria over the parameter space

Table 1: Fluid properties for simulation cases.

ρ_l	ρ_g	μ_l	μ_g	σ	D_0	U_0
(kg/m ³)	(kg/m ³)	(Pa s)	(Pa s)	(N/m)	(m)	(m/s)
1000	1.2	0.001	0.000018	0.072	$5.8 \times 10^{-3} - 5 \times 10^{-6}$	1.34 – 88.02

Table 2: Range of dimensionless parameters for simulation cases.

We	Re	Oh	r
$\rho_g U_0^2 D_0 / \sigma$	$\rho_g U_0 D_0 / \mu_g$	$\mu_l / \sqrt{\rho_l D_0 \sigma}$	ρ_g / ρ_l
0.1 – 10	10 – 1000	0.0012 – 0.0861	0.0012

of interest, see Fig. 1(b)). Among them, 92 cases will be used for data-driven model development, and are further split randomly into training and validation sets by an 80:20 ratio. Training sets are used to train the model and validation sets will ensure the model’s robustness by preventing the over-fitting of the training data. The remaining 10 cases will be used as the testing set which will provide the unbiased evaluation of the trained model. The simulation cases used as training, validation, and testing datasets are detailed in the [Appendix A](#).

3. Interface-resolved simulations

3.1. Simulation methods

Interface-resolved simulations were performed for the selected cases to generate the data to train and test the data-driven model. The two-phase interfacial flows are governed by the incompressible Navier-Stokes equations with surface tension,

$$\rho \left(\frac{\partial u_i}{\partial t} + u_i \frac{\partial u_j}{\partial x_j} \right) = -\frac{\partial p}{\partial x_i} + \frac{\partial}{\partial x_j} \left[\mu \left(\frac{\partial u_i}{\partial x_j} + \frac{\partial u_j}{\partial x_i} \right) \right] + \sigma \kappa \delta_s n_i, \quad (1)$$

$$\frac{\partial u_i}{\partial x_i} = 0. \quad (2)$$

where ρ, u_i, p, μ represent density, velocity, pressure and viscosity, respectively. The Dirac distribution function δ_s is localized on the interface. The surface

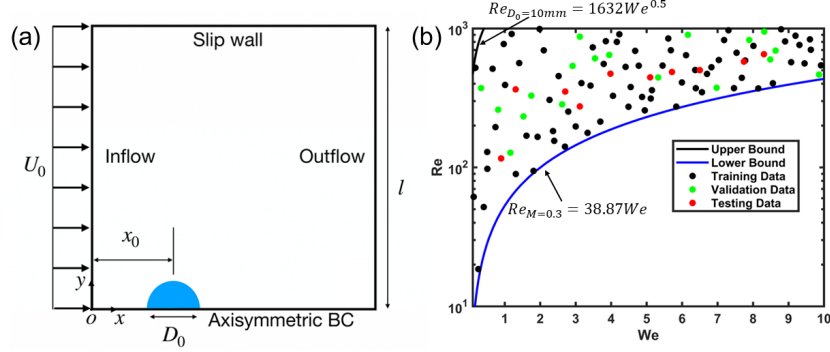


Figure 1: (a) Schematic of simulation domain and (b) parameter space of interest in the We - Re plane, where We and Re are in linear and log scales, respectively.

tension coefficient is denoted by σ , while κ and n_i represent the curvature and normal vector of the interface.

The gas and liquid phases are distinguished by the liquid volume fraction c , the evolution of which follows the advection equation:

$$\frac{\partial c}{\partial t} + u_i \frac{\partial c}{\partial x_i} = 0. \quad (3)$$

After spatial discretization, the cells with pure liquid or gas will exhibit $c = 1$ and 0, respectively, while for cells containing the gas-liquid interface, c is a fractional number. The density and viscosity are both defined based on the arithmetic mean

$$\rho = \rho_l c + \rho_g (1 - c), \quad (4)$$

$$\mu = \mu_l c + \mu_g (1 - c). \quad (5)$$

The present simulations are conducted using the open-source solver *Basilisk*. The governing equations are solved using a finite-volume method. The projection method is used to incorporate the incompressibility condition. Sharp interfaces separating the two phases are traced by solving the advection equation via a mass-momentum consistent geometric Volume-of-Fluid (VOF) method [3, 59]. The balanced-force method is used to discretize the singular surface tension term in the momentum equation [34]. The interface curvature required to calculate surface tension is computed based on the height-function (HF) method

[34]. The staggered-in-time discretization of the volume fraction/density and pressure leads to a formally second-order-accurate time discretization [34]. An quadtree mesh is used to discretize the 2D computational domain, which allows for adaptive mesh refinement (AMR) in user-defined regions. The mesh adaptation is based on the wavelet estimate of the discretization errors of specified variables [54]. Validation of the numerical methods and the solver *Basilisk* in resolving drop deformation and breakup can be found in our previous studies [58, 41, 42, 40, 24, 9, 10].

3.2. Simulation setup

The computational domain is shown in Fig. 1(a). The velocity of the drop and the gas in the domain is initially zero. The velocity boundary condition is invoked on the left boundary of the domain, with a pressure outflow boundary condition invoked on the right boundary. Due to the incompressibility condition, the gas is suddenly accelerated to U_0 in an infinitesimal time (one time step in the simulation). The bottom is the axis and the top is a slip wall. The computational domain has an edge length of $l = 64D_0$, and the drop is initially placed $x_0 = 3D_0$ away from the left boundary. The computational domain is discretized by a quadtree mesh, which is dynamically adapted based on the wavelet estimates of the discretization errors of the liquid volume fraction and the velocity components. The minimum cell size Δ is controlled by the maximum refinement level \mathcal{L} , i.e., $\Delta = l/2^{\mathcal{L}}$. In the present study, $\mathcal{L} = 13$ is used, corresponding to 128 minimum quadtree cells across the initial drop diameter, i.e., $N = D_0/\Delta = 128$. The grid-refinement study, to be discussed in section 4.3, confirms that the mesh resolution is sufficient.

4. Simulation results and data processing

4.1. General behavior

The time evolution of the pressure fields and drop surface for different We and Re are shown in Fig. 2. The cases in (a), (b), and (c) are for $(We, Re) =$

(0.13, 61.42), (0.97, 772.89), and (9.60, 834.65), which represent low- We -low- Re , low- We -high- Re , and high- We -high- Re regimes, respectively. The high stagnation pressure near the windward and leeward poles of the drop drives radial flow towards the periphery, leading to the flattening of the drop in the streamwise direction [55, 15]. The corresponding Oh for cases (a), (b), and (c) are 0.011, 0.0025, and 0.0071, respectively. Due to the low Oh , surface tension is the dominant force resisting drop deformation. It is evident that cases with low We show only mild deformation throughout the process, whereas, for the case with high We , the deformation is more pronounced, and the drop transitions from a sphere to a flat disk, as seen in Fig. 2(c). Since We is below the critical value, surface tension is sufficient to revert the drop to an elongated shape, causing it to deform in an oscillatory manner. Although cases (a) and (b) have low We and thus similar drop shapes, their Re values are markedly different, leading to distinct wake structures and consequently different drag forces on the drop.

4.2. Drop shape characterization

To characterize the shape of the drop, we employ the spherical coordinate system, and the radius on the drop surface can be expressed as a function of the colatitude θ and time t , i.e., $R = R(\theta, t)$. The instantaneous drop shape can be decomposed into axisymmetric spherical harmonic modes, represented by Legendre polynomials P_n

$$\frac{R(\theta, t) - R_0}{R_0} = \sum_{n=0}^{\infty} C_n(t) P_n(\cos(\theta)), \quad (6)$$

where $R_0 = D_0/2$ is the volume-based radius, C_n represents the coefficient for the mode n , which varies over time. For the current problem, keeping modes with $n \leq 10$ is sufficient to accurately represent the drop shape for all cases and all time. Given the instantaneous shape of the drop, C_n can be computed by the Legendre-Fourier transform

$$C_n(t) = \frac{2n+1}{2} \int_{-1}^1 \frac{R(\theta, t) - R_0}{R_0} P_n(\cos(\theta)) d(\cos(\theta)). \quad (7)$$

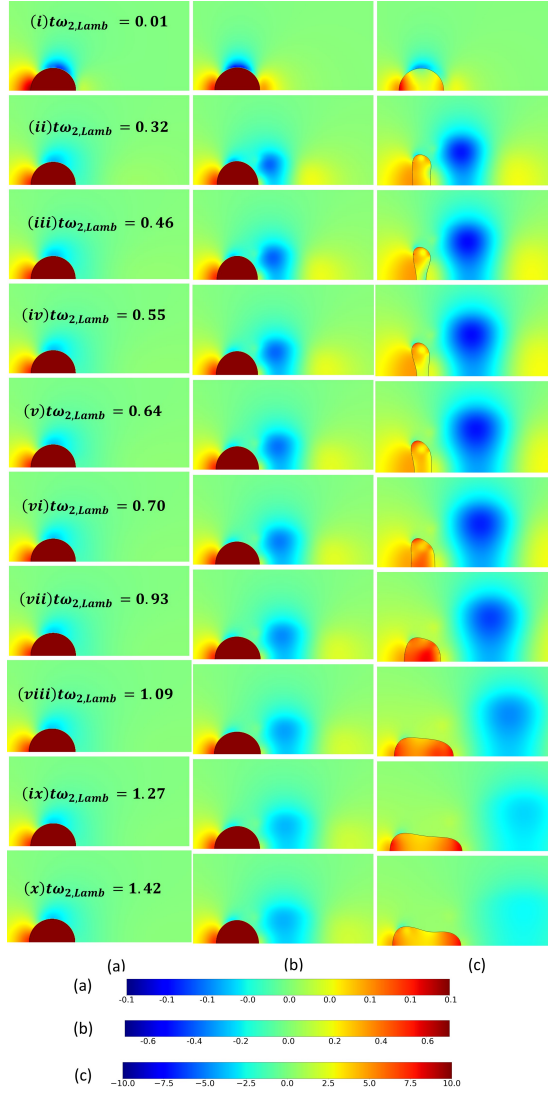


Figure 2: Temporal evolutions of the pressure fields for three representative cases with different We and Re . (a) $We = 0.13$, $Re = 61.42$, (b) $We = 0.97$, $Re = 772.89$, (c) $We = 9.60$, $Re = 834.65$.

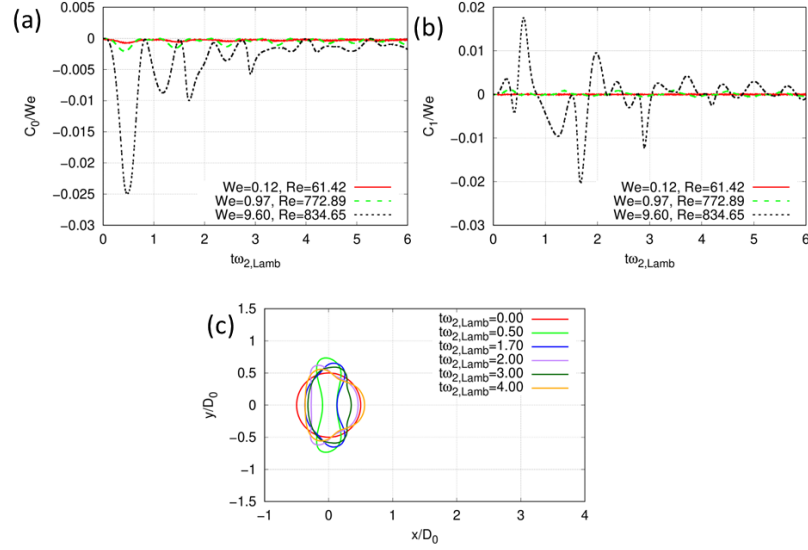


Figure 3: Temporal evolutions of (a) C_0 and (b) C_1 for three representative cases with different We and Re . (c) Time snapshots of the drop shapes for the case $We = 9.60$ and $Re = 834.65$.

When the drop deformation amplitude is small, $C_0 = 0$ if the volume is constant and $C_1 = 0$ if $R(\theta, t)$ is defined based on the drop center. However, when the drop deformation amplitude is high, as for cases with high We , C_0 and C_1 are not identical to zero when the centroid is used as the origin of the coordinate system, see Figs. 3(a) and (b). The deviations from zero are more profound for the case $We = 9.60$, for which the drop deforms more significantly, which can be observed from the snapshots of the drop shapes shown in Fig. 3(c). As the deformation amplitude decreases over time, the magnitudes for C_0 and C_1 also reduce. The results here indicate that it is necessary to include C_0 and C_1 for shape characterization.

4.3. Grid refinement study

To verify that the mesh resolution is sufficient to resolve the drop shape oscillation, a grid-refinement study is performed using the same representative cases shown in Fig. 2. Since these cases represent the corners in the parameter space of interest, convergence of results for these cases will guarantee the mesh

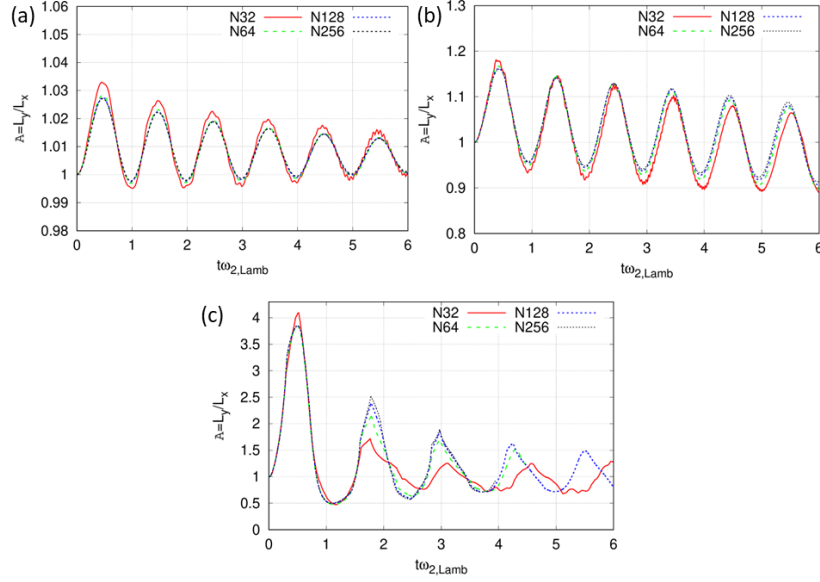


Figure 4: Temporal evolutions of the aspect ratios ($A = L_y/L_x$) for different levels of mesh refinement $N = D_0/\Delta_{min} = 32 - 256$ for three representative cases with different We and Re . (a) $We = 0.13$, $Re = 61.42$, (b) $We = 0.97$, $Re = 772.89$, (c) $We = 9.60$, $Re = 834.65$.

is fine enough for other cases considered.

The time evolutions of the aspect ratio, $A = L_y/L_x$, where L_x and L_y are the streamwise and lateral widths of the drop, for different cases and mesh resolutions, are shown in Fig. 4. Four different mesh refinement levels have been tested, $\mathcal{L} = 11, 12, 13$, and 14 , which correspond to $N = D_0/\Delta = 32, 64, 128$, and 256 , respectively. Time has been normalized with the Lamb frequencies of the dominant second mode $\omega_{2,lamb}$. The Lamb frequency of the n^{th} axisymmetric mode is given as [20]

$$\omega_{n,Lamb} = \sqrt{\frac{(n-1)n(n+1)(n+2)\sigma}{[(n+1)\rho_l + n\rho_g]R_0^3}}. \quad (8)$$

The results for $N = 128$ and 256 match very well, indicating the mesh $N = 128$ is sufficient to yield converged results, which is used for the parametric simulations.

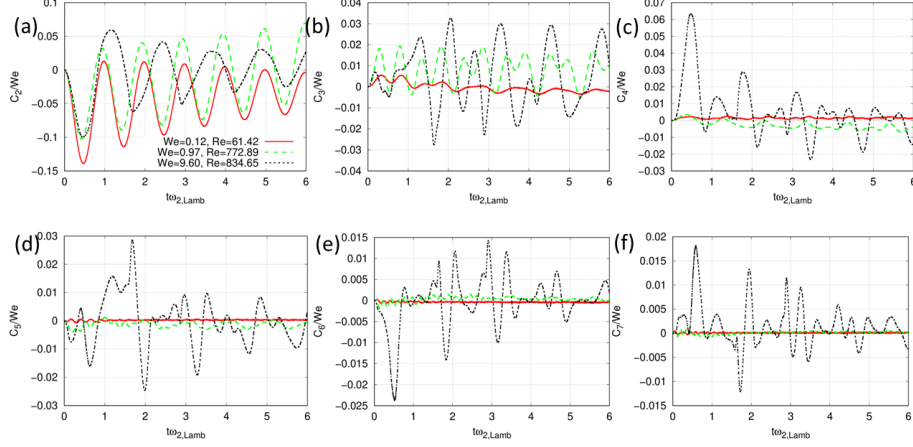


Figure 5: Temporal evolutions of the modal coefficients C_2 to C_7 for three representative cases.

4.4. Temporal evolutions of modal coefficients

The temporal evolutions of the Fourier-Legendre coefficients for modes $n = 2 - 7$ for different We and Re are plotted in Fig. 5. As the amplitude of the modal coefficient variation increases with We , we have plotted the ratio of C_n to We instead. The differences in the results between different cases are reduced for C_n/We , which also helps to improve the accuracy of the data-driven model.

All the modal coefficients are initially zero since the drop is spherical at $t = 0$. As the drop starts to deform, C_n varies over time. It is shown that the oscillation of C_2 exhibits a single frequency. For low We cases, the frequency is close to that of the 2nd Lamb mode, while a lower frequency is observed for the high $We = 9.60$ case. Furthermore, the equilibrium state of the C_2 oscillation is not zero, indicating the equilibrium shape is not a perfect sphere. The time evolutions of the coefficients for modes $n > 2$ are more complicated, in particular for the high We case, due to the non-linear effects [6, 5, 58]. It is difficult to model the time evolutions of each mode using simple explicit functions, as can be done for small-amplitude drop oscillations [58].

4.5. Temporal evolutions of drag coefficient

The aerodynamic drag causes the drop to accelerate along the streamwise direction. The mean x-velocity of the drop is calculated by the integration of the velocity and VOF fields,

$$u_d = \frac{\int c u dV}{\int c dV} \quad (9)$$

based on which the drop acceleration can be calculated as du_d/dt , and the drag coefficient is evaluated as

$$C_D = \frac{2m_d}{\rho_g(U_0 - u_d)^2 \pi R^2} \frac{du_d}{dt} \quad (10)$$

where m_d is the mass of the drop. Here, C_D is defined based on the instantaneous relative velocity $(U_0 - u_d)$, and the drop frontal area (πR^2) estimated by the lateral radius R . We normalize the drag coefficient with the standard drag correlation for spherical particle corresponding to Re ,

$$C_{D,std} = \frac{24}{Re}(1 + 0.15Re^{0.687}) + \frac{0.42}{1 + \frac{42500}{Re^{1.16}}} \quad (11)$$

The time evolutions of C_D for different We and Re are shown in Fig. 6. The three cases shown are the same cases shown in Figs. 2 and 4. Initially C_D is much higher than $C_{D,std}$ due to the impulsive acceleration at time zero and the resulting unsteady forces (added-mass and Basset history force) [25]. The drag coefficient will approach the steady drag after the transition phase, the duration of which is dictated by the viscous unsteady time scale. For the case (a) with low $We = 0.13$ and $Re = 61.42$, it is seen that $C_D/C_{D,std}$ reaches a plateau, about 0.82, see Fig. 6. In contrast, C_D for case (b) oscillates in time and the oscillation frequency matches with that for the shape oscillation. The increase in C_D oscillation amplitude is attributed to the increase of We and the resulting stronger drop shape deformation, see Fig. 4. Compared to case (a), the wake structure for case (b) also varies as Re increases significantly, see Fig. 2, which contributes to the lower plateau value of C_D . For the case (c) with high $We = 9.60$, C_D exhibits a more complex oscillation with multiple

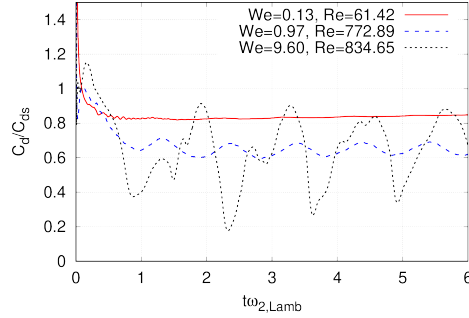


Figure 6: Temporal evolutions of drag coefficients for three representative cases with different We and Re .

frequencies and larger amplitude, which is due to the large-amplitude multi-mode shape oscillations, see Fig. 4. The oscillation in C_D with a frequency similar to the shape oscillation clearly demonstrates that the drag and shape evolutions are closely coupled. Therefore, it is necessary to incorporate the drop shape evolution into the data-driven model to accurately predict the drag.

4.6. Effect of We and Re on aspect ratio and dominant frequency

The complex dynamics for drops in finite We and Re regimes make it challenging to model drop shape and drag evolutions through conventional physics-based approaches. This complexity is evident in the oscillation amplitude and frequency. Given that oscillation amplitude generally decreases over time due to viscous dissipation, the maximum aspect ratio, $A_{\max} = \max(|L_y/L_x|)$, typically occurring during the first oscillation, is used to represent the oscillation amplitude [5]. The results for the maximum aspect ratio A_{\max} across all simulated cases are summarized in Fig. 7. It is observed that A_{\max} primarily varies with We . The variation of A_{\max} with We is nonlinear and typically follows a quadratic function, as depicted in Fig. 7(a). The dependence of A_{\max} on Re is generally weak, as seen in Fig. 7(b). For a given We , Oh is inversely proportional to Re , so the weak dependence on Re also indicates that the effect of Oh on the oscillation amplitude is small for the ranges of parameters considered.

While multiple modes with different frequencies are present, the dominant

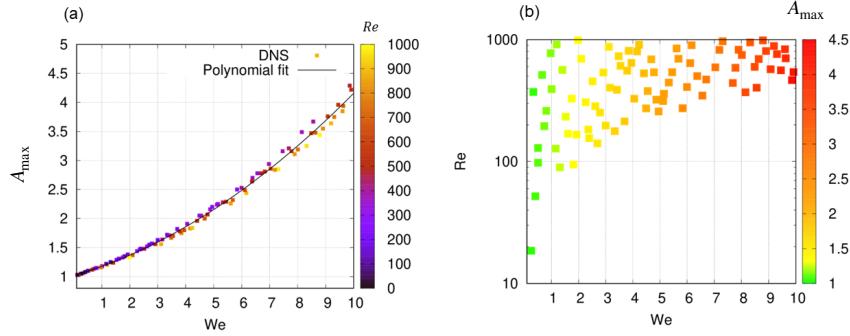


Figure 7: (a) Variation of the maximum aspect ratio $A_{\max} = \max(L_y/L_x)$ as a function of We for all cases simulated. (b) Variation of the maximum aspect ratio A_{\max} on the We - Re plane.

mode is the second mode for all cases, as depicted in the spectra for two representative cases shown in Fig. 8(b). The normalized dominant frequency $\omega/\omega_{2,Lamb}$ is plotted as a function of A_{\max} and Re in Fig. 8(a). A decrease in frequency is observed as A_{\max} increases, attributable to the increase in We , as shown in Fig. 7(a). The dispersion of data points is due to the limited spectral resolution to identify the dominant frequency. Improving spectral resolution would require running simulations for a much longer time, which is beyond the scope of this study. Nonetheless, a general decreasing trend of $\omega/\omega_{2,Lamb}$ with We or A_{\max} is evident. This decrease in frequency, due to nonlinear effects in large-amplitude oscillation, aligns reasonably well with the Tsamopoulos and Brown (TB) nonlinear model when A_{\max} is moderate [53]. However, as A_{\max} increases, significant deviations from the TB model are observed, as also observed in previous numerical studies [5].

The uncertainties in identifying the dominant frequency render the results somewhat noisy, making it challenging to clearly demonstrate the impact of Re on the dominant frequency. For high We cases, oscillation frequency changes over time; as the oscillation amplitude decreases, the nonlinear effect on frequency is reduced. Consequently, the frequency during the initial oscillation may slightly differ from that reflected in the spectrum, which accounts for all oscillations, as shown in Fig. 8(b).

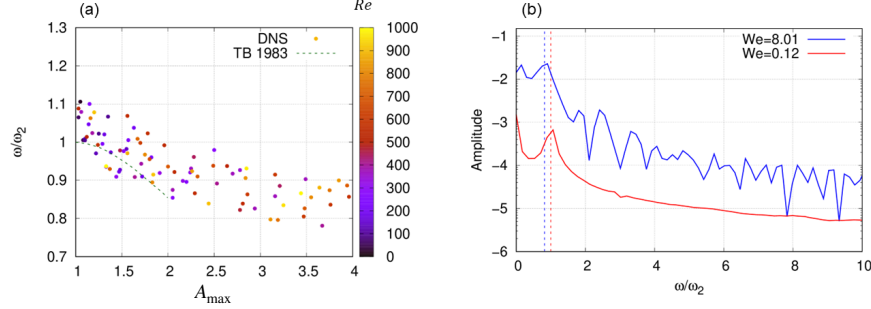


Figure 8: (a) Variation of dominant frequency with maximum aspect ratio $A_{\max} = \max(L_y/L_x)$. The color represents Re . (b) Frequency spectra for two cases with different We . The dashed vertical lines indicate the frequency measured based on the first oscillation.

In summary, these results demonstrate the difficulty of predicting drop shape oscillation through physics-based approaches, highlighting the necessity for data-driven modeling.

5. Machine-learning data-driven models

5.1. Model overview

The purpose of the present data-driven model is to predict the temporal evolutions of the drop shape and the drag based on the initial flow conditions and the fluid properties, characterized by the dimensionless parameters like We and Re . Such a model can be used in Lagrangian spray simulations to predict the motion and shape of individual drops without solving the flows on the drop scale. As described above, the drop shape is characterized by the modal coefficients $C_0 - C_{10}$ and the drop drag is represented by the drag coefficient. In the simulations, the above quantities are calculated and collected at a fixed timestep $\Delta t_{model} \sqrt{\sigma/\rho_l D_0^3} = 0.01$ for model training and testing. The simulations have been run to $t_{sim} \omega_{2,Lamb} = 10.17$ (equivalent to $t_{sim} \sqrt{\sigma/\rho_l D_0^3} = 8.00$) in general. As a result, there are in total 800 temporal datapoints of modal and drag coefficients for one sample (*i.e.*, simulation case). For some cases with $We \geq 7$, the drop will leave the domain before the specified end time, then for those cases the simulations were stopped as the drop reaches a distance of $2D_0$ from the

right boundary. There are 24 cases in the training set that fall into this category and the minimum simulation time is $t_{sim}\omega_{2,Lamb} = 6.43$. For those cases, we will have smaller numbers of datapoints. Note that the timestep Δt_{model} in the dataset for model development is larger than the timestep Δt_{sim} used in the simulation, and the downsampling is done to provide a compressed dataset without aliasing errors.

The overall machine-learning model is depicted in Fig. 9. The model comprises two multi-layer perceptron (MLP) models. The first model is the drop shape model, which predicts future modal coefficients based on the history of modal coefficients and the dimensionless parameters We and Re . The second model is the drop drag model, which uses the history of both modal and drag coefficients, We and Re as inputs to predict future drag coefficients. The rationale for separating the models is to reduce input redundancy, as the history of C_D is not required for predicting the future shape of the drop. Thus, the first model exclusively uses the history of modal coefficients.

Normalization of data to minimize differences across various cases enhances training efficiency. The modal coefficients defining the drop shape are normalized by We , i.e., $C_n^* = C_n / We$, because the amplitude variation of C_n increases with We . Similarly, the drag coefficient is normalized by the standard drag for the corresponding Re , i.e., $C_D^* = C_D / C_{D,std}$.

5.2. Nonlinear Auto-Regressive models with eXogenous inputs (NARX) recurrent neural network

The Nonlinear Auto-Regressive with eXogenous inputs (NARX) recurrent neural network is a machine-learning model that predicts the system's outputs based on a nonlinear combination of previous outputs and exogenous input parameters [21, 22]. This model has demonstrated its accuracy in modeling complex, time-dependent systems, as indicated in prior research [12, 29, 7]. In the present study, the physical parameters Re and We serve as the exogenous inputs. The NARX model can be expressed as a mapping of future predictions of the vector of quantities of interest $\mathbf{y} = (C_0, C_1, \dots, C_{10}, C_D)$ from the history

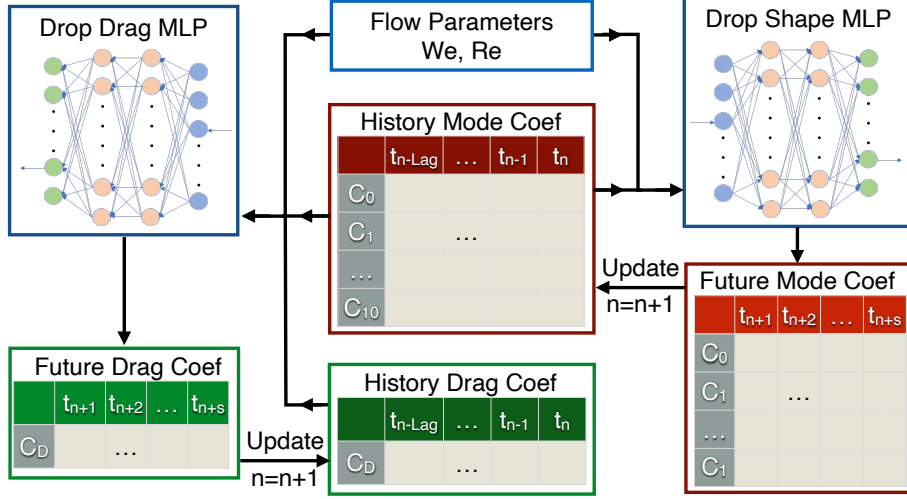


Figure 9: Overall modeling strategy.

data and exogenous inputs, i.e.,

$$\mathbf{y}(t_n, \dots, t_{n+1}, t_{n+s-1}) = F[\mathbf{y}(t_{n-1}), \dots, \mathbf{y}(t_{n-lag}), Re, We] \quad (12)$$

where *stride* (*s*) and *lag* are model hyperparameters that represent the number of future and history timesteps used in each prediction, respectively.

5.3. Model training and testing

A NARX neural network can be open-loop or closed-loop. In the present model, the training process is open-loop, for which the simulation data from the history steps are used as inputs to predict the future steps. The open-loop training process for the drop shape model is shown in Fig. 10(a). Here, *lag* = 50 and *s* = 10 were used, which means that the modal coefficients from the preceding 50 timesteps are utilized to predict the values for the subsequent 10 timesteps. Consequently, one input “dataset” to the drop shape MLP consists of 552 inputs, including the 11 modal coefficients for the 50 history steps, plus *We* and *Re*, and the MLP output consists of 110 outputs, specifically the modal coefficients for the future 10 steps. Examples for the input-output pairs of two subsequent datasets are depicted in Fig. 10(a). For the dataset using modal coefficients for $t_{n-50}, t_{n-49}, \dots, t_n$ as inputs, the corresponding outputs for the future steps

are $t_{n+1}, t_{n+2}, \dots, t_{n+10}$, while the subsequent dataset uses the modal coefficients for $t_{n-49}, t_{n-48}, \dots, t_n, t_{n+1}$ to predict the values for $t_{n+2}, t_{n+3}, \dots, t_{n+11}$. At time zero, there is no “history” available. Then synthetic data for $t < 0$ are created, where the modal coefficients are taken to be zero, i.e., $C_{0,1,\dots,10}(t < 0) = 0$, and the normalized drag coefficient is set to one, i.e., $C_D/C_{D,std}(t < 0) = 1$, according to the initial spherical shape of the drop. As a result, for one sample in the training set, there will be 800 datasets for the 800 timesteps.

The data for all samples with different combinations of We and Re will be combined to the input and output tensors. Then the paired input and output tensors will be shuffled and separated into batches for training. The loss function is the mean squared error (MSE) between model predictions and the ground truth values for the output tensor for one batch. The final loss for an epoch is the average loss across all batches. The MLP comprises 8 hidden layers. Details about the neurons in each layer and other hyperparameters such as learning rate, and batch size are provided in Table 3. Early stopping based on evaluating the validation dataset is used to prevent overfitting of the model on training data.

The testing of the trained model will be closed loop, see Fig. 10(b). The predicted outputs for the future 10 timesteps will be fed back as inputs to the model. For example, the previous predicted modal coefficients for $t_{n-50}, t_{n-49}, \dots, t_n$ will be used to predict the future values at $t_{n+1}, t_{n+2}, \dots, t_{n+10}$, which will then be used as the next input dataset to the MLP, i.e., the modal coefficients for $t_{n-50}, t_{n-39}, \dots, t_{n+10}$, to predict the values for $t_{n+11}, t_{n+12}, \dots, t_{n+20}$. Similar subsequent predictions will be made. Similar to the training process, synthetic data for $t < 0$ will be used to initiate the model prediction. Therefore, the present model is recurrent and will only require Re and We to autonomously predict the temporal evolutions of the modal coefficients.

The drop drag model architecture is similar the shape model. The MLP for the drop drag has the same number of hidden layers and neurons as the drop shape MLP. The only difference is that, the time history data of C_d^* were added to the inputs. As a result, the drop drag model takes historical values of modal and drag coefficients as temporal inputs and We and Re as exogenous inputs,

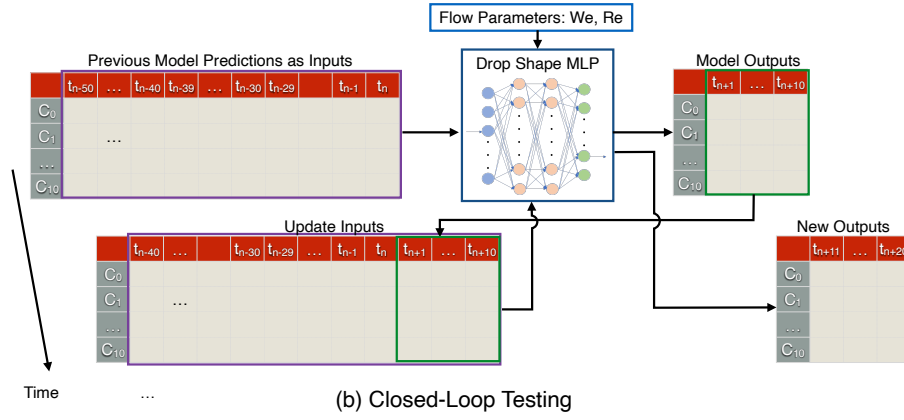
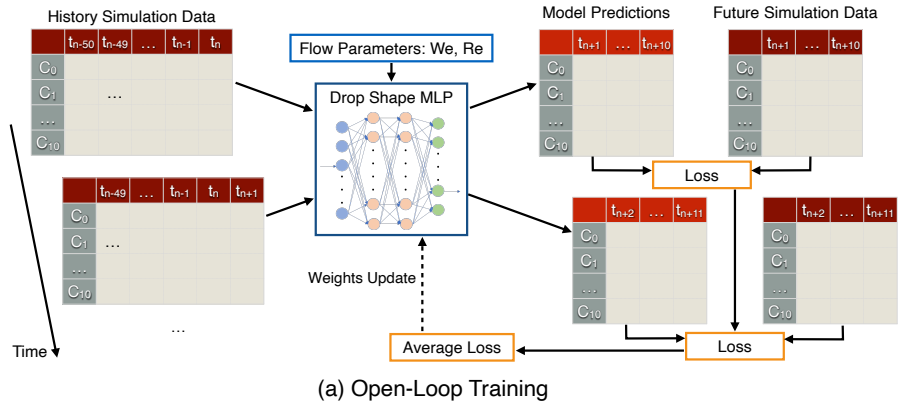


Figure 10: Schematic flowchart to show the (a) open-loop training and (b) closed-loop testing processes for the drop shape model.

Table 3: Parameters for the NARX neural network model.

<i>Hyperparameters</i>	<i>Value</i>
<i>Total Number of Inputs for One Dataset for Drop Shape MLP</i>	552
<i>Total Number of Inputs for One Dataset for Drop Drag MLP</i>	602
<i>Total Number of Outputs for One Dataset for Drop Shape MLP</i>	110
<i>Total Number of Outputs for One Dataset for Drop Drag MLP</i>	10
<i>Number of Hidden Layers</i>	8
<i>Total Number of Neurons in Hidden Layers</i>	4450
<i>Batch Size</i>	16
<i>Learning Rate</i>	10^{-5}
<i>Weight Decay</i>	10^{-7}
<i>Lag</i>	50
<i>Stride, s</i>	10
<i>Maximum Epoch Number</i>	1000
<i>Optimizer</i>	<i>AdamW</i>
<i>Loss Function</i>	<i>Mean square error</i>

to predict future values C_d^* . In total, one dataset for the drop drag MLP has 602 inputs and 10 outputs, see table 3. Similar to the shape model, drag model also uses open-loop data flow during training and closed loop for testing.

The average simulation time for one case is about 165 core-hours using an AMD EPYC 7002 processor. The average training times per epoch for the drop shape and drag MLP networks are about 19.32 and 16.03 seconds, respectively, using an NVIDIA RTX 2070 GPU. The number of epochs varies with cases, and the maximum number of epochs is 1000. Once the model is trained, it takes 0.45-0.58 seconds to predict the time evolutions of modal and drag coefficients.

5.4. Model evaluation

The model performance will be evaluated using error metrics, including the Mean Relative Errors (MRE) for the modal coefficients (C_{MRE}) and drag coefficients ($C_{d_{MRE}}$). As the modal coefficients enable reconstruction of the drop shape, specifically $R(\theta)$ in spherical coordinates, we also assess the MRE for the drop radius (R_{MRE}). The error expressions are as follows:

$$C_{MRE} = \frac{1}{N} \sum_{n=1}^N \frac{\|\hat{\mathbf{C}} - \mathbf{C}\|_F}{\|\mathbf{C}\|_F} \quad (13)$$

$$C_{d_{MRE}} = \frac{1}{N} \sum_{n=1}^N \frac{\|\hat{\mathbf{C}}_d - \mathbf{C}_d\|_2}{\|\mathbf{C}_d^*\|_2} \quad (14)$$

$$R_{MRE} = \frac{1}{N} \sum_{n=1}^N \frac{\|\hat{\mathbf{R}} - \mathbf{R}\|_F}{\|\mathbf{R}\|_F} \quad (15)$$

where N denotes the total number of data points evaluated. Variables with and without $\hat{}$ represent ground truth (simulation data) and model predictions, respectively. The matrix \mathbf{C} includes the modal coefficients and all timesteps and samples, while \mathbf{R} and \mathbf{C}_d are vectors for the drop radius at various colatitudes and drag coefficient at different timesteps for all samples. Subscripts F and 2 denote Frobenius and L_2 norm errors for matrices and vectors, respectively.

Table 4: Summary of MRE result for different datasets.

Datasets	R_{MRE}	C_{MRE}	$C_{d_{MRE}}^*$
<i>Training Sets</i>	0.80%	9.62%	1.28%
<i>Validation Sets</i>	0.84%	8.36%	1.30%
<i>Testing Sets</i>	0.78%	8.91%	0.88%

6. Data-driven model predictions

6.1. Model prediction for drop shape deformation

The model predictions of the modal coefficients (C_0 - C_{10}) for two cases in the testing dataset, i.e., $(We, Re) = (0.89, 116.12)$ and $(8.31, 652.63)$, representing low and high We regimes in the parameter space, are shown in Figs. 11 and 12, respectively. It is noteworthy that these two test cases were never “seen” by the model. The predicted time evolutions of all the modal coefficients align remarkably well with the simulation results. The high-order modal coefficients exhibit complicated oscillations, which are accurately captured by the model. Though some discrepancies were observed at later times for the higher-order modes, like C_5 - C_{10} , their amplitudes are small compared to the dominant mode C_2 . As a result, the discrepancies have a negligible effect on the overall drop shape. Figure 13 shows the drop shapes at different times reconstructed from the modal coefficients, illustrating that the predictions for both cases closely match the simulation results. This excellent agreement confirms the model’s ability to accurately predict the drop shape evolutions for different We and Re .

Table 4 summarizes the radius and modal coefficients prediction errors for training, validation and testing datasets. The MRE in modal coefficients (C_{MRE}), around 8–9%, may seem high. However, the high-order modes, which contribute significantly to this error, see Fig. 11, have minor impacts on the drop shape. Thus, the relatively higher errors in the high-order modal coefficients do not significantly affect the accuracy of the predicted drop shape, which is reflected by the MRE for the drop radius (R_{MRE}). It is observed that R_{MRE} values are less than 1% for all datasets.

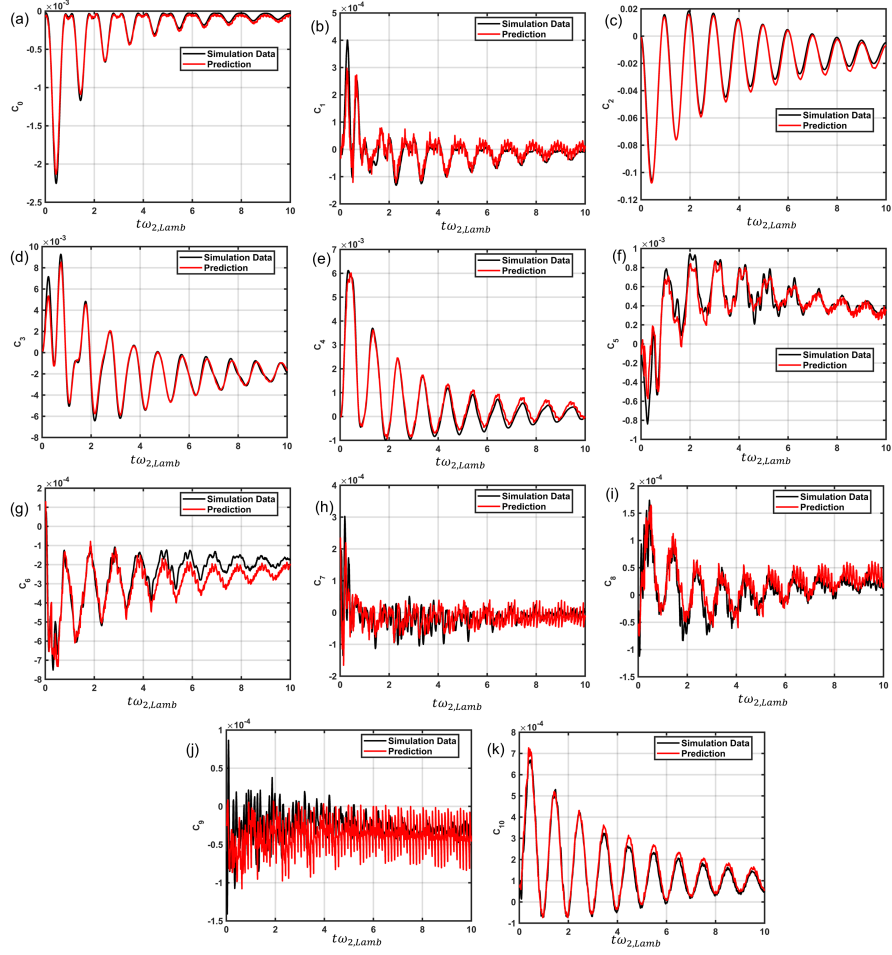


Figure 11: Comparison between model predictions of modal coefficients (C_0 - C_{10}) and simulation data for the test case ($Re = 116.12$, $We = 0.89$)

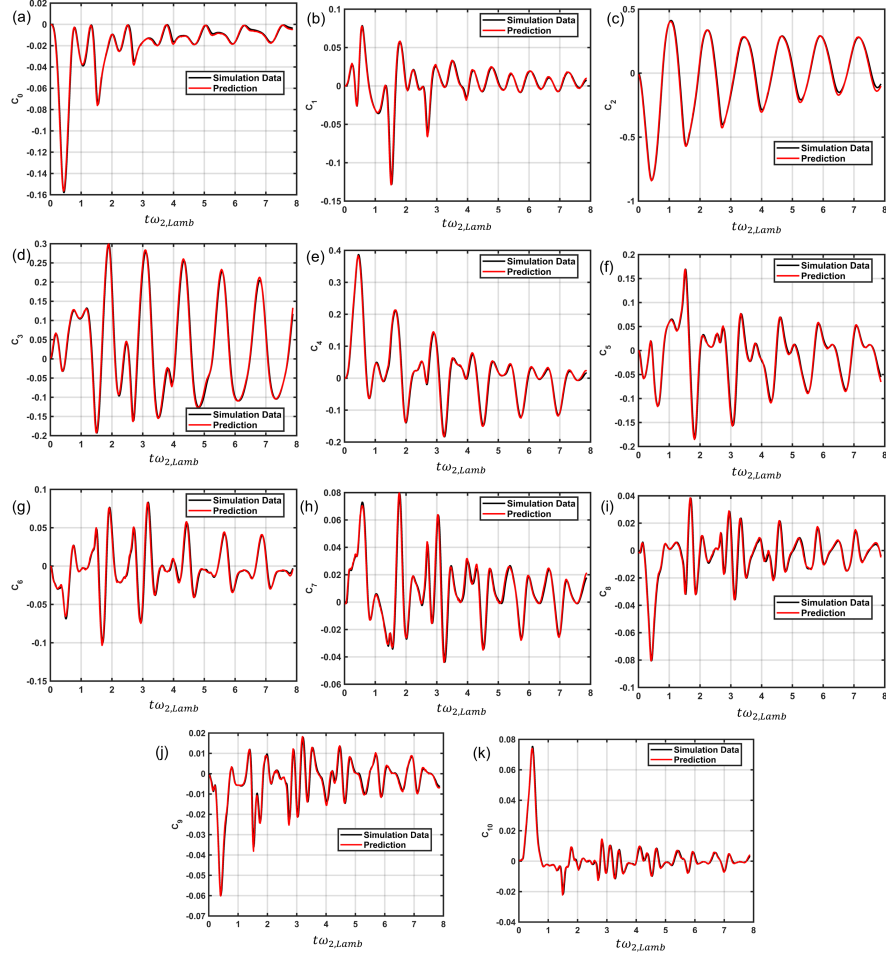


Figure 12: Comparison between model predictions of modal coefficients (C_0 - C_{10}) and simulation data for the test case ($Re = 652.63$, $We = 8.31$)

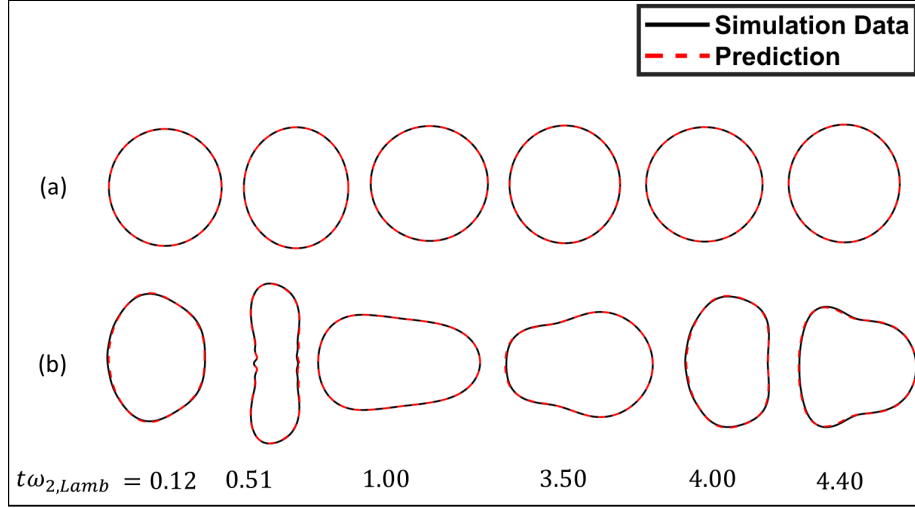


Figure 13: Comparison between model predictions of drop shapes and simulation data for the test cases (a) $Re = 116.12$, $We = 0.89$, and (b) $Re = 652.63$, $We = 8.31$.

The values of R_{MRE} for all 10 cases in the testing dataset are given in Table 5. It can be observed that R_{MRE} increases with We . The highest error, 1.59%, is associated with the case with $Re = 652.63$ and $We = 8.307$. As We increases, the drop deforms more significantly and the drop shape is also more complex. The magnitude of the modal coefficients also increases with We . As a result, the error in modal coefficients has a greater influence on the drop shape for cases with higher We .

6.2. Model prediction for drop drag coefficient

With the drop shape model validated, the predictions of the modal coefficients are now incorporated into the drop drag model to predict the time evolution of the drag coefficient. Figure 14 shows the time evolutions of C_d^* predicted by the present model for two test cases, $(We, Re) = (0.89, 116.12)$ and $(8.31, 652.63)$. Again, the model predictions agree very well with the simulation data for both cases for all time. Due to the drop shape oscillation, C_d^* evolves in an oscillatory manner, and the model well captures the frequency and magnitude of C_d^* .

Table 5: MRE results for all cases in the test set.

Cases	Re	We	R_{MRE}	C_{MRE}	$C_{d_{MRE}}^*$
1	116.13	0.898	0.16%	9.02%	0.47%
2	364.52	1.307	0.26%	8.44%	0.35%
3	351.40	2.705	0.42%	8.09%	0.42%
4	274.80	3.117	0.35%	7.19%	0.28%
5	472.41	3.979	0.65%	8.32%	0.62%
6	444.77	5.099	0.80%	9.14%	0.73%
7	486.27	5.714	1.11%	10.91%	1.10%
8	501.24	6.499	1.08%	9.27%	1.12%
9	577.14	7.741	1.34%	9.19%	1.73%
10	652.63	8.307	1.59%	9.55%	1.99%
<i>Mean</i>			0.78%	8.91%	0.88%

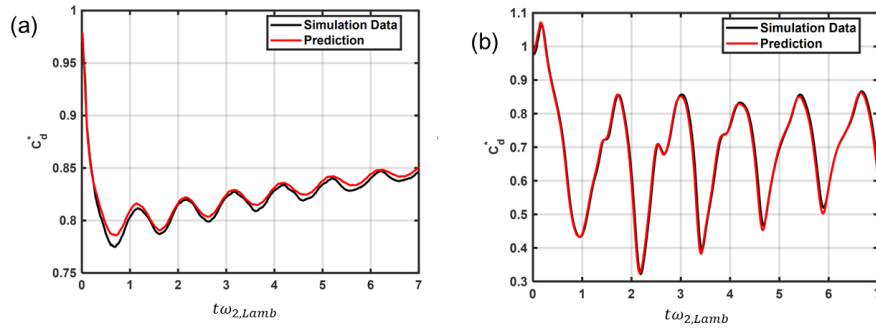


Figure 14: Comparison between model predictions of C_d^* and simulation data for test cases (a) $We = 0.89$, $Re = 116$ and (b) $We = 8.31$, $Re = 652.63$.

The prediction errors of C_d^* for different datasets are shown in Table 4. Due to the error propagation from the shape model to the drag model, the error in drag coefficient is slightly higher than that for the drop radius, but $C_{d_{MRE}}^*$ remains lower than 1% for the testing set. The values of $C_{d_{MRE}}^*$ for all cases in the testing set can be found in Table 5. Similar to the error in the drop shape, the error in the drag increases with We , and the values of $C_{d_{MRE}}^*$ and R_{MRE} are quite similar. The maximum error of C_d^* is 1.99%, which is associated with the case with $Re = 652.63$ and $We = 8.307$. The similarity between $C_{d_{MRE}}^*$ and R_{MRE} affirms that accurate prediction the drop shape evolution is necessary to well predict the drag and drop motion.

7. Conclusions

A data-driven model has been developed in the present study to predict the shape and drag evolutions of a freely-moving drop in a uniform stream. Assuming the drop fluid and the surrounding gas are water and air, with the drop initially spherical, the key parameters are the Weber (We) and Reynolds (Re) numbers, defined based on the initial relative velocity and the drop diameter. The present study focuses on the subcritical Weber number regime, in which drops will deform but not break. The significant deformation of the drop influences the interaction between the drop and the surrounding gas flow. As a result, accurately predicting the drag and the resulting motion of the drop requires rigorous prediction of the drop shape evolutions. The complex interplay between drop shape deformation and drag makes conventional physics-based models difficult, so a data-driven approach based on Non-linear Auto-Regressive with eXogenous inputs (NARX) recurrent neural network is adopted.

To provide data for model development, parametric interface-resolved 2D-axisymmetric simulations were performed for 102 cases of different combinations of We and Re numbers in the parameter space of interest. The geometric volume-of-fluid (VOF) method is used to resolve the sharp interface, and an adaptive quadtree mesh with the minimum cell size equivalent to 128 cells

across the initial drop diameter is used in the simulation. To characterize the instantaneous drop shapes, the drop radius as a function of the colatitude is decomposed into spherical harmonic modes. Assuming the drop is axisymmetric, only the axisymmetric modes are considered. The amplitudes of the modal coefficients decrease with the mode number, and a truncation is made at the mode number 10. Eventually, the temporal data for the modal and drag coefficients are collected from the simulations. The modal coefficients are normalized by We and the drag coefficient is normalized by the standard drag for spherical particles to reduce the differences across cases.

The overall model consists of two NARX models. The first model, the drop shape model, takes the history of modal coefficients as temporal inputs, along with We and Re as exogenous inputs, and predicts the modal coefficients at future timesteps. The second model, the drop drag model, uses the history of modal and drag coefficients, along with We and Re , as inputs and then predicts the drag coefficients in future steps. The overall simulation data is split into training (92 cases) and testing sets (10 cases). The NARX model training is open-loop, meaning the history simulation data are used as inputs, while testing of the model is done in a closed-loop manner, where the predictions are fed back as inputs, so that the model prediction is recurrent. The model accurately predicts the evolution of both the modal and drag coefficients for both low and high We cases. The modal coefficients can be used to reconstruct the drop shape, and prediction errors are also measured on the reconstructed drop radius as a function of the colatitude. The drag coefficient evolves in time in an oscillatory manner due to the drop shape oscillation, and the model predictions agree very well with the simulation data for cases in the testing set. The mean relative errors in the predictions of drop radius and drag coefficient generally increase with We . The maximum errors in the testing cases are 1.59% and 1.99% for drop radius and drag coefficient, respectively.

Appendix A. Parameters for simulation dataset

Figure A.15 shows the initial drop diameter D_0 and the free-stream velocity U_0 for all 102 simulation cases, along with the corresponding values of key dimensionless parameters We , Re , and Oh . Other fluid properties are kept constant. The simulation cases are then split into training, validation, and testing datasets, as indicated.

Acknowledgments

This research was supported by ACS-PRF (#62481-ND9) and NSF (#1942324). The authors also acknowledge the ACCESS program for providing the computational resources that have contributed to the research results reported in this paper.

References

- [1] B. Abramzon, W. A. Sirignano, Droplet vaporization model for spray combustion calculations, *Int. J. Heat Mass Transfer* 32 (1989) 1605–1618.
- [2] S. Apte, M. Gorokhovski, P. Moin, LES of atomizing spray with stochastic modeling of secondary breakup, *Int. J. Multiphase Flow* 29 (2003) 1503–1522.
- [3] T. Arrufat, M. Cialesi-Esposito, D. Fuster, Y. Ling, L. Malan, S. Pal, R. Scardovelli, G. Tryggvason, S. Zaleski, A momentum-conserving, consistent, Volume-of-Fluid method for incompressible flow on staggered grids, *Comput. Fluids* 215 (2020) 104785.
- [4] S. Balachandar, A scaling analysis for point particle approaches to turbulent multiphase flows, *Int. J. Multiphase Flow* 35 (2009) 801–810.
- [5] O. A. Basaran, Nonlinear oscillations of viscous liquid drops, *J. Fluid Mech.* 241 (1992) 169–198.

Cases	D ₀ (m)	U ₀ (m/s)	We	Re	Oh	Dataset
1	5.60E-05	3.09E+01	0.90	116.13	0.0157	Test
2	1.40E-04	5.19E+01	6.50	501.24	0.0098	Test
3	1.70E-04	3.08E+01	2.71	351.40	0.0090	Test
4	1.60E-04	5.37E+01	7.74	577.14	0.0093	Test
5	9.10E-05	4.54E+01	3.12	274.80	0.0124	Test
6	1.90E-04	5.09E+01	8.31	652.63	0.0085	Test
7	2.10E-04	3.37E+01	3.98	472.41	0.0081	Test
8	1.50E-04	4.59E+01	5.10	444.77	0.0098	Test
9	1.60E-04	4.70E+01	5.71	486.27	0.0095	Test
10	3.80E-04	1.43E+01	1.31	364.52	0.0060	Test
11	5.00E-06	5.53E+01	0.26	18.56	0.0525	Train
12	2.50E-05	3.15E+01	0.41	51.88	0.0237	Train
13	5.85E-03	1.34E+00	0.17	521.31	0.0015	Train
14	1.10E-04	8.20E+00	0.13	61.43	0.0111	Train
15	1.20E-04	1.57E+01	0.51	129.22	0.0106	Train
16	4.90E-05	6.09E+01	3.00	197.19	0.0169	Train
17	1.90E-04	1.52E+01	0.74	195.07	0.0085	Train
18	2.30E-04	3.54E+01	4.78	539.46	0.0078	Train
19	2.80E-05	7.65E+01	2.70	141.04	0.0224	Train
20	3.80E-05	6.17E+01	2.39	155.35	0.0192	Train
21	5.80E-04	2.08E+01	4.16	800.49	0.0049	Train
22	5.70E-04	1.03E+01	1.01	392.26	0.0049	Train
23	1.80E-05	7.68E+01	1.81	94.37	0.0275	Train
24	3.50E-05	7.52E+01	3.34	177.37	0.0198	Train
25	9.90E-05	4.95E+01	4.05	327.39	0.0118	Train
26	4.60E-05	6.92E+01	3.69	213.51	0.0173	Train
27	7.30E-04	1.86E+01	4.23	908.35	0.0044	Train
28	2.30E-03	5.04E+00	0.97	772.89	0.0025	Train
29	5.00E-05	7.69E+01	4.95	257.37	0.0166	Train
30	3.10E-04	2.22E+01	2.52	454.43	0.0067	Train
31	6.40E-04	1.90E+01	3.85	809.82	0.0047	Train
32	7.00E-05	2.09E+01	0.51	97.71	0.0141	Train
33	3.80E-04	2.71E+01	4.68	689.98	0.0060	Train
34	6.70E-05	3.81E+01	1.61	169.11	0.0145	Train
35	5.40E-05	4.64E+01	1.93	165.93	0.0161	Train
36	8.50E-04	9.99E+00	1.41	563.57	0.0041	Train
37	8.00E-05	6.06E+01	4.87	321.50	0.0132	Train
38	1.50E-03	5.13E+00	0.66	512.88	0.0030	Train
39	6.20E-05	6.57E+01	4.49	273.27	0.0149	Train
40	2.30E-05	5.86E+01	1.31	89.64	0.0246	Train
41	2.61E-03	5.24E+00	1.20	912.94	0.0023	Train
42	2.40E-04	3.33E+01	4.41	529.11	0.0076	Train
43	1.20E-04	4.80E+01	4.55	378.82	0.0108	Train
44	8.70E-04	1.21E+01	2.10	696.15	0.0040	Train
45	8.50E-05	4.43E+01	2.79	252.18	0.0128	Train
46	1.90E-04	3.13E+01	3.16	404.22	0.0085	Train
47	5.30E-05	5.17E+01	2.36	182.64	0.0162	Train
48	1.60E-04	2.96E+01	2.26	306.09	0.0095	Train
49	5.80E-04	1.90E+01	3.48	731.46	0.0049	Train
50	1.70E-04	3.53E+01	3.42	387.79	0.0092	Train
51	1.86E-03	8.00E+00	1.98	990.90	0.0027	Train
52	3.10E-04	2.73E+01	3.79	555.74	0.0067	Train
53	7.20E-05	6.53E+01	5.12	313.30	0.0139	Train
54	9.40E-05	5.73E+01	5.15	359.67	0.0121	Train
55	2.50E-04	3.81E+01	6.11	642.01	0.0074	Train
56	4.80E-05	8.52E+01	5.83	273.78	0.0170	Train
57	4.80E-04	3.01E+01	7.31	970.12	0.0054	Train
58	2.70E-04	4.60E+01	9.60	834.65	0.0071	Train
59	1.50E-04	5.07E+01	6.37	502.34	0.0097	Train
60	6.90E-05	7.54E+01	6.56	347.75	0.0142	Train
61	1.40E-04	6.35E+01	9.07	571.60	0.0101	Train
62	1.90E-04	4.75E+01	7.04	592.93	0.0086	Train
63	3.20E-04	3.26E+01	5.68	697.02	0.0066	Train
64	2.60E-04	4.28E+01	8.01	749.37	0.0073	Train
65	1.00E-04	5.87E+01	5.99	408.74	0.0115	Train
66	4.10E-04	3.57E+01	8.79	986.23	0.0058	Train
67	6.90E-05	8.03E+01	7.46	371.80	0.0141	Train
68	9.50E-05	6.96E+01	7.68	441.43	0.0121	Train
69	7.10E-05	8.49E+01	8.56	403.26	0.0140	Train
70	1.20E-04	5.69E+01	6.70	470.86	0.0106	Train
71	6.30E-05	8.80E+01	8.15	370.28	0.0148	Train
72	1.90E-04	5.48E+01	9.63	702.66	0.0085	Train
73	2.70E-04	4.41E+01	8.90	807.08	0.0071	Train
74	4.80E-04	2.65E+01	5.61	846.87	0.0054	Train
75	2.30E-04	4.89E+01	9.31	760.80	0.0077	Train
76	2.00E-04	4.03E+01	5.45	540.40	0.0083	Train
77	1.70E-04	5.29E+01	7.78	587.92	0.0091	Train
78	3.60E-04	3.48E+01	7.18	825.20	0.0063	Train
79	1.20E-04	6.75E+01	9.45	560.35	0.0106	Train
80	1.10E-04	7.31E+01	9.91	542.26	0.0112	Train
81	8.10E-05	6.87E+01	6.39	371.58	0.0131	Train
82	1.50E-04	5.19E+01	6.83	525.85	0.0096	Train
83	3.20E-04	4.15E+01	9.20	886.20	0.0066	Train
84	2.20E-04	4.51E+01	7.54	668.58	0.0079	Train
85	1.55E-03	3.60E+00	0.34	372.10	0.0030	Validation
86	3.70E-04	2.17E+01	2.91	537.73	0.0061	Validation
87	3.10E-04	1.25E+01	0.81	260.13	0.0067	Validation
88	2.30E-04	2.13E+01	1.75	328.27	0.0078	Validation
89	1.30E-04	2.62E+01	1.53	232.89	0.0102	Validation
90	4.00E-04	2.45E+01	3.95	644.91	0.0059	Validation
91	3.90E-04	2.33E+01	3.55	609.28	0.0059	Validation
92	9.20E-04	1.43E+01	3.12	872.77	0.0039	Validation
93	1.20E-04	3.68E+01	2.62	284.25	0.0110	Validation
94	5.30E-05	3.63E+01	1.16	127.62	0.0162	Validation
95	3.20E-04	3.82E+01	7.89	826.41	0.0065	Validation
96	7.50E-05	7.45E+01	6.97	374.43	0.0136	Validation
97	4.90E-04	2.74E+01	6.16	900.04	0.0053	Validation
98	8.20E-05	8.47E+01	9.86	465.63	0.0130	Validation
99	1.60E-04	5.67E+01	8.48	598.23	0.0094	Validation
100	1.40E-04	4.80E+01	5.33	444.11	0.0100	Validation
101	2.10E-04	4.98E+01	8.63	692.99	0.0082	Validation
102	4.10E-04	3.50E+01	8.32	949.25	0.0058	Validation

Figure A.15: Parameters of all simulation cases and corresponding dataset.

- [6] E. Becker, W. J. Hiller, T. A. Kowalewski, Experimental and theoretical investigation of large-amplitude oscillations of liquid droplets, *J. Fluid Mech.* 231 (1991) 189–210.
- [7] S. Benouar, M. Kadir-Talha, F. Seoane, Time-series NARX feedback neural network for forecasting impedance cardiography ICG missing points: a predictive model, *Front. Physiol.* 14 (2023) 1181745.
- [8] K. Bergeles, Y. Hardalupas, A. M. K. P. Taylor, On the transient flow inside and around a deforming millimetre class oil droplet falling under the action of gravity in stagnant air, *Phys. Fluids* 30 (2018) 013305.
- [9] B. Boyd, S. Becker, Y. Ling, Simulation and modeling of the vaporization of a freely moving and deforming drop at low to moderate Weber numbers, *Int. J. Heat Mass Transfer* 218 (2023) 124735.
- [10] B. Boyd, Y. Ling, A consistent volume-of-fluid approach for direct numerical simulation of the aerodynamic breakup of a vaporizing drop, *Comput. Fluids* 254 (2023) 105807.
- [11] D. R. Guildenbecher, C. López-Rivera, P. E. Sojka, Secondary atomization, *Exp. Fluids* 46 (2009) 371.
- [12] M. Haris, M. N. Hasan, S. Qin, State of health prediction of supercapacitors using multi-trend learning of NARX neural network, *Mater. Today Sustain.* 20 (2022) 100201.
- [13] L. He, D. K. Tafti, A supervised machine learning approach for predicting variable drag forces on spherical particles in suspension, *Powder Technol.* 345 (2019) 379–389.
- [14] L.-P. Hsiang, G. M. Faeth, Near-limit drop deformation and secondary breakup, *Int. J. Multiphase Flow* 18 (1992) 635–652.
- [15] I. M. Jackiw, N. Ashgriz, On aerodynamic droplet breakup, *J. Fluid Mech.* 913 (2021) A33.

- [16] S. S. Jain, N. Tyagi, R. S. Prakash, R. V. Ravikrishna, G. Tomar, Secondary breakup of drops at moderate Weber numbers: Effect of Density ratio and Reynolds number, *Int. J. Multiphase Flow* 117 (2019) 25–41.
- [17] D. D. Joseph, J. Belanger, G. S. Beavers, Breakup of a liquid drop suddenly exposed to a high-speed airstream, *Int. J. Multiphase Flow* 25 (1999) 1263–1303.
- [18] V. Kulkarni, D. R. Guildenbecher, P. E. Sojka, Secondary Atomization of Newtonian Liquids in the Bag Breakup Regime: Comparison of Model Predictions to Experimental Data, in: *ICLASS 2012, 12th International Conference on Liquid Atomization and Spray Systems*, 2012.
- [19] B. Lalanne, S. Tanguy, F. Risso, Effect of rising motion on the damped shape oscillations of drops and bubbles, *Phys. Fluids* 25 (2013) 112107.
- [20] H. Lamb, *Hydrodynamics*, Cambridge University Press, 1932.
- [21] T. Lin, B. Horne, P. Tino, C. Giles, Learning long-term dependencies is not as difficult with NARX networks, in: *Proceedings of 9th Annual Conference on Neural Information Processing Systems (NIPS)*, vol. 8, 577–583, 1995.
- [22] T. Lin, B. G. Horne, P. Tino, C. L. Giles, Learning long-term dependencies in NARX recurrent neural networks, *IEEE Trans. Neural Netw. Learn. Syst.* 7 (1996) 1329–1338.
- [23] Y. Lin, J. Palmore Jr, Effect of droplet deformation and internal circulation on drag coefficient, *Phys. Rev. Fluids* 7 (2022) 123602.
- [24] Y. Ling, T. Mahmood, Detailed numerical investigation of the drop aerobreakup in the bag breakup regime, *J. Fluid Mech.* 972 (2023) A28.
- [25] Y. Ling, M. Parmar, S. Balachandar, A Scaling Analysis of Added-Mass and History Forces and Their Coupling in Dispersed Multiphase Flows, *Int. J. Multiphase Flow* 57 (2013) 102–114.

- [26] J. Manin, M. Bardi, L. M. Pickett, R. N. Dahms, J. C. Oefelein, Microscopic investigation of the atomization and mixing processes of diesel sprays injected into high pressure and temperature environments, *Fuel* 134 (2014) 531–543.
- [27] F. Marcotte, S. Zaleski, Density contrast matters for drop fragmentation thresholds at low Ohnesorge number, *Phys. Rev. Fluids* 4 (2019) 103604.
- [28] M. R. Maxey, J. J. Riley, Equation of motion for a small rigid sphere in a nonuniform flow, *Phys. Fluids* 26 (1983) 883–889.
- [29] J. M. P. Menezes Jr, G. A. Barreto, Long-term time series prediction with the NARX network: An empirical evaluation, *Neurocomputing* 71 (2008) 3335–3343.
- [30] C. A. Miller, L. E. Scriven, The oscillations of a fluid droplet immersed in another fluid, *J. Fluid Mech.* 32 (1968) 417–435.
- [31] P. J. O’Rourke, A. A. Amsden, The TAB method for numerical calculation of spray droplet breakup, Tech. Rep. Tech. Rep. LA-UR-2105., Los Alamos National Laboratory, 1987.
- [32] M. G. Pai, S. Subramaniam, Modeling interphase turbulent kinetic energy transfer in Lagrangian-Eulerian spray computations, *Atomization Spray* 16 (2006) 807–826.
- [33] M. Pilch, C. A. Erdman, Use of breakup time data and velocity history data to predict the maximum size of stable fragments for acceleration-induced breakup of a liquid drop, *Int. J. Multiphase Flow* 13 (1987) 741–757.
- [34] S. Popinet, An accurate adaptive solver for surface-tension-driven interfacial flows, *J. Comput. Phys.* 228 (16) (2009) 5838–5866.
- [35] A. Prosperetti, Normal-mode analysis for the oscillations of a viscous-liquid drop in an immiscible liquid, *J. Mecanique* 19 (1980) 149–182.

- [36] A. A. Ranger, J. A. Nicholls, Aerodynamic shattering of liquid drops., AIAA J. 7 (1969) 285–290.
- [37] L. Rayleigh, On the capillary phenomena of jets, Proc. R. Soc. Lond. 29 (1879) 71–97.
- [38] W. H. Reid, The oscillations of a viscous liquid drop, Q. Appl. Maths 18 (1960) 86–89.
- [39] N. Rimbart, S. C. Escobar, R. Meignen, M. Hadj-Achour, M. Gradeck, Spheroidal droplet deformation, oscillation and breakup in uniform outer flow, J. Fluid Mech. 904 (2020) A15.
- [40] J. Sakakeeny, C. Deshpande, S. Deb, J. L. Alvarado, Y. Ling, A model to predict the oscillation frequency for drops pinned on a vertical planar surface, J. Fluid Mech. 928 (2021) A28.
- [41] J. Sakakeeny, Y. Ling, Natural oscillations of a sessile drop on flat surfaces with mobile contact lines, Phys. Rev. Fluids 5 (2020) 123604.
- [42] J. Sakakeeny, Y. Ling, Numerical study of natural oscillations of supported drops with free and pinned contact lines, Phys. Fluids 33 (2021) 062109.
- [43] S. Sharma, A. P. Singh, S. S. Rao, A. Kumar, S. Basu, Shock induced aerobreakup of a droplet, J. Fluid Mech. 929 (2021) A27.
- [44] B. Siddani, S. Balachandar, Point-particle drag, lift, and torque closure models using machine learning: hierarchical approach and interpretability, Phys. Rev. Fluids 8 (2023) 014303.
- [45] B. Siddani, S. Balachandar, R. Fang, Rotational and reflectional equivariant convolutional neural network for data-limited applications: Multiphase flow demonstration, Phys. Fluids 33 (2021) 103323.
- [46] B. Siddani, S. Balachandar, W. C. Moore, Y. Yang, R. Fang, Machine learning for physics-informed generation of dispersed multiphase flow using

- generative adversarial networks, *Theor. Comp. Fluid Dyn.* 35 (2021) 807–830.
- [47] K. Tang, T. Adcock, W. Mostert, Bag film breakup of droplets in uniform airflows, *J. Fluid Mech.* 970 (2023) A9.
 - [48] T. G. Theofanous, G. J. Li, On the physics of aerobreakup, *Phys. Fluids* 20 (2008) 052103.
 - [49] T. G. Theofanous, G. J. Li, T.-N. Dinh, Aerobreakup in rarefied supersonic gas flows, *J. Fluid Eng.-T. ASME* 126 (2004) 516–527.
 - [50] T. G. Theofanous, G. J. Li, T.-N. Dinh, C.-H. Chang, Aerobreakup in disturbed subsonic and supersonic flow fields, *J. Fluid Mech.* 593 (2007) 131–170.
 - [51] T. G. Theofanous, V. V. Mitkin, C. L. Ng, The physics of aerobreakup. III. Viscoelastic liquids, *Phys. Fluids* 25 (2013) 032101.
 - [52] S. S. Tiwari, E. Pal, S. Bale, N. Minocha, A. W. Patwardhan, K. Nandakumar, J. B. Joshi, Flow past a single stationary sphere, 2. Regime mapping and effect of external disturbances, *Powder Technol.* 365 (2020) 215–243.
 - [53] J. A. Tsamopoulos, R. A. Brown, Nonlinear oscillations of inviscid drops and bubbles, *J. Fluid Mech.* 127 (1983) 519–537.
 - [54] J. A. van Hooft, S. Popinet, C. C. van Heerwaarden, S. J. A. van der Linden, S. R. de Roode, B. J. H. van de Wiel, Towards adaptive grids for atmospheric boundary-layer simulations, *Bound.-Layer Meteor.* 167 (2018) 421–443.
 - [55] E. Villermaux, B. Bossa, Single-drop fragmentation determines size distribution of raindrops, *Nature Phys.* 5 (2009) 697–702.
 - [56] Z. Y. Wan, P. Karnakov, P. Koumoutsakos, T. P. Sapsis, Bubbles in turbulent flows: Data-driven, kinematic models with history terms, *Int. J. Multiphase Flow* 129 (2020) 103286.

- [57] G. Yun, D. Kim, H. Choi, Vortical structures behind a sphere at subcritical Reynolds numbers, *Phys. Fluids* 18 (2006) 015102.
- [58] B. Zhang, Y. Ling, P.-H. Tsai, A.-B. Wang, S. Popinet, S. Zaleski, Short-term oscillation and falling dynamics for a water drop dripping in quiescent air, *Phys. Rev. Fluids* 4 (2019) 123604.
- [59] B. Zhang, S. Popinet, Y. Ling, Modeling and detailed numerical simulation of the primary breakup of a gasoline surrogate jet under non-evaporative operating conditions, *Int. J. Multiphase Flow* 130 (2020) 103362.